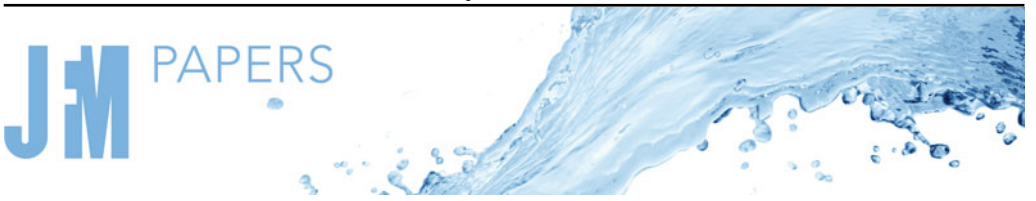
J. Fluid Mech. (2026), *vol.* 1042, A14, doi:10.1017/jfm.2026.11955



A new receptivity mechanism for the second-mode instability in hypersonic boundary layers

Hongtian Qiu[1], **Xianyang Jiang**[1] **and Cun-Biao Lee**[1,2]

[1]School of Mechanics and Engineering Science, State Key Laboratory for Turbulence and Complex Systems, Peking University, Beijing 100871, PR China

[2]Beijing Institute of Mathematical Sciences and Applications, Beijing 101408, PR China

Corresponding authors: Xianyang Jiang, xyjmh@pku.edu.cn; Cun-Biao Lee, cblee@mech.pku.edu.cn

(Received 24 March 2026 UTC; revised 14 July 2026 UTC; accepted 17 July 2026 UTC)

Direct numerical simulations of the flow over a compound delta-wing model reveal a novel receptivity mechanism for the second-mode instability in hypersonic boundary layers. This mechanism involves disturbances that propagate obliquely upward from the wall, interact with the shock wave and reflect back into the boundary layer. Detailed analysis indicates that this process strongly modulates high-frequency instabilities, such as the second mode, while exerting minimal influence on low-frequency cross-flow and first-mode disturbances. Upon re-entry into the boundary layer, the reflected disturbances cause rapid, stepwise amplification of the internal second mode, demonstrating that the mechanism modulates and enhances boundary-layer instability. Further analysis shows that a phase-locked mechanism is involved in these interactions. The identification of this receptivity mechanism offers new insights into hypersonic boundary-layer transition.

Key words: boundary layer receptivity, hypersonic flow

1. Introduction

The transition in the boundary layers is fundamentally initiated by the receptivity process, which describes how external disturbances enter the boundary layer and excite internal unstable waves (Morkovin 1969; Lee & Chen 2019). Typically, there is a significant disparity in the spatial and temporal scales between external forcing and internal instability

© The Author(s), 2026. Published by Cambridge University Press. This is an Open Access article, distributed under the terms of the Creative Commons Attribution licence (https://creativecommons.org/licenses/by/4.0/), which permits unrestricted re-use, distribution and reproduction, provided the original article is properly cited.

https://doi.org/10.1017/jfm.2026.11955 Published online by Cambridge University Press

modes within the boundary layer. Therefore, the primary objective of receptivity studies is to identify a scale-convergence mechanism that tunes the scales of external perturbations to match those of internal waves (Fedorov 2011). Understanding this mechanism can provide an initial disturbance amplitude for subsequent linear stability analyses and improve the accuracy of transition prediction.

Early theoretical investigations into receptivity utilised high-order asymptotic expansions to study the localised scattering of acoustic and vortical disturbances by surface geometry variations (Goldstein 1985). These foundational studies established that localised geometric features play a crucial role in providing the rapid spatial modulation between external disturbances and internal waves. In low-speed flows, the disturbance transformation process typically occurs near the leading edge, as it is not only the first region to encounter external disturbances but also exhibits the strongest receptivity (Saric *et al.* 2002). Consequently, it is generally emphasised that disturbances propagate downstream from the leading edge within the boundary layer. However, recent advancements have revealed the existence of self-organised, forward-propagating oblique waves upstream of the leading edges of blunt plates (Yang *et al.* 2025). These structures can evolve and re-enter the boundary layer, exhibiting a direct physical link to transition-related coherent structures (Lee & Jiang 2019; Chen *et al.* 2026). This discovery highlights the critical importance of receptivity mechanisms, by which external waves penetrate a boundary layer downstream of the leading edge and modulate the development of flow structures therein.

In hypersonic flows, free stream disturbances interact with the shock wave, generating a complex spectrum of acoustic, vorticity and entropy waves (McKenzie & Westphal 1968). Among these, receptivity to acoustic waves has been studied most extensively, as it directly triggers the excitation and synchronisation of fast/slow modes within the boundary layer (Fedorov & Khokhlov 1991). Extensive numerical results have confirmed that the generation of internal boundary-layer waves, such as the first and second modes, is mainly driven by acoustic waves behind the bow shock (Zhong & Wang 2012). Based on this, the majority of studies focus on the process by which free stream disturbances pass through the shock wave, enter the boundary layer near the leading edge and subsequently propagate downstream (Maslov *et al.* 2001). However, for configurations with blunt leading edges, an entropy layer forms behind the shock wave. Disturbances can propagate along the entropy layer and penetrate the boundary layer further downstream to induce unstable modes (Wan *et al.* 2020). The transition reversal, a phenomenon where the transition location is initially delayed and then rapidly advances upstream with increasing bluntness, is also considered to be contributed by the entropy layer and non-modal instability, as discussed in Guo *et al.* (2025). Their subsequent work (Guo 2025) revealed that entropic, slow acoustic, fast acoustic and vortical waves can all generate the 'streamwise streak-turbulent spot' two-stage transition scenario. This indicates that receptivity mechanisms occurring downstream of a leading edge are equally vital for hypersonic transition, yet comprehensive studies addressing these phenomena remain severely limited.

In this paper, direct numerical simulations (DNS) are employed to identify a novel receptivity mechanism in hypersonic boundary layers, whereby second-mode frequency disturbances enter the boundary layer downstream of the leading edge. The results demonstrate that this mechanism plays a significant role in the amplification and development of disturbances within the boundary layer. The paper is organised as follows. The numerical set-up is described in § 2. Results are presented in § 3, followed by a discussion in § 4. Conclusions are drawn in § 5.

https://doi.org/10.1017/jfm.2026.11955 Published online by Cambridge University Press

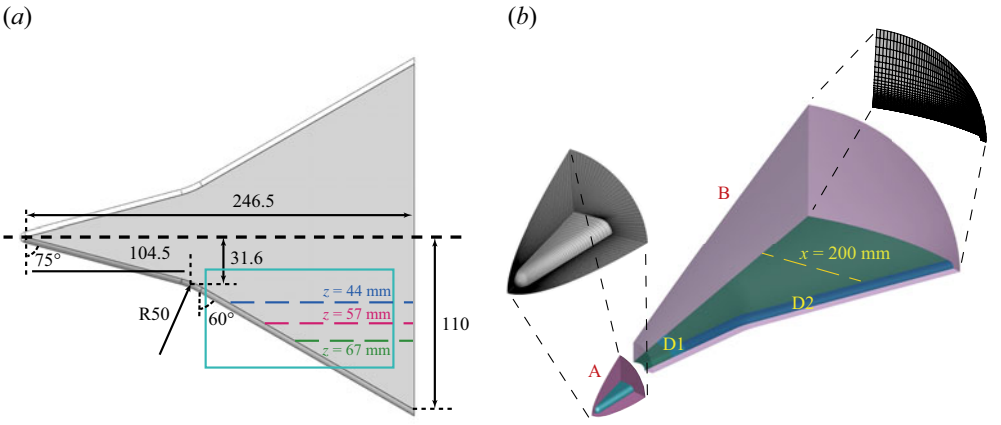


Figure 1. (*a*) Schematic diagram of the simulation model. (*b*) Computational grid configuration, divided into two parts, zone A and zone B, with D1 and D2 being the two disturbance injection regions in zone B.

2. Model and methodology

2.1. *Model configuration and simulation set-up*

The compound delta-wing model under consideration has a length of 250 mm, a thickness of 7 mm and features a rounded leading edge, as shown in figure 1(*a*). The sweep angle changes from 75° to 60° at $x = 100$ mm, where a 50 mm circular arc smoothly connects two sides. The free stream conditions are defined by a Mach number of 6, a static pressure of 395 Pa, a total temperature of 420 K and a unit Reynolds number of 1.0×10^7 m^{-1}. The DNS is conducted in two sequential steps, as shown in figure 1(*b*): resolving the nose region of the delta wing (zone A), followed by the downstream main body encompassing the bow shock (zone B). The corresponding grid dimensions ($N_x \times N_y \times N_z$) are $200 \times 250 \times 100$ for zone A and $1400 \times 250 \times 320$ for zone B.

In zone A, the convective fluxes are discretised using the MUSCL scheme, while the viscous terms are discretised via a fourth-order central difference scheme. Uniform free stream conditions are imposed at the inflow boundary, and an extrapolation condition is applied at the outflow. Symmetry conditions are enforced along both the centreline and the leading edge. In zone B, the Steger–Warming flux-vector splitting method is utilised to evaluate the convective fluxes, which are subsequently discretised using a seventh-order weighted essentially nonoscillatory (WENO) scheme. An eighth-order central difference scheme is adopted for the viscous terms, and time integration is advanced via a third-order total variation diminishing (TVD) Runge–Kutta method. The inflow and upper boundary conditions are prescribed using natural neighbour interpolation from the converged solution of zone A. Symmetry conditions are retained at the centreline and leading edge, alongside an extrapolation condition at the outflow. Finally, an isothermal, no-slip condition is prescribed on the solid surface.

To verify grid independence, three grid resolutions are evaluated: low ($1000 \times 100 \times 200$), medium ($1700 \times 150 \times 300$) and high ($2000 \times 200 \times 400$). In all cases, the minimum wall-normal grid spacing, Δy^+_{min}, is maintained below 1 to ensure adequate near-wall resolution. A comparison of the base-flow profiles obtained from these grids is presented in figure 2(*a–c*). The wall-normal distance y, cross-flow velocity w_t, tangential velocity u_t and temperature T are normalised by the 99 % boundary-layer thickness y_{99}, the $0.1u_0$, u_0 and $10T_0$, respectively, where u_0 and T_0 are the free stream velocity and static

https://doi.org/10.1017/jfm.2026.11955 Published online by Cambridge University Press

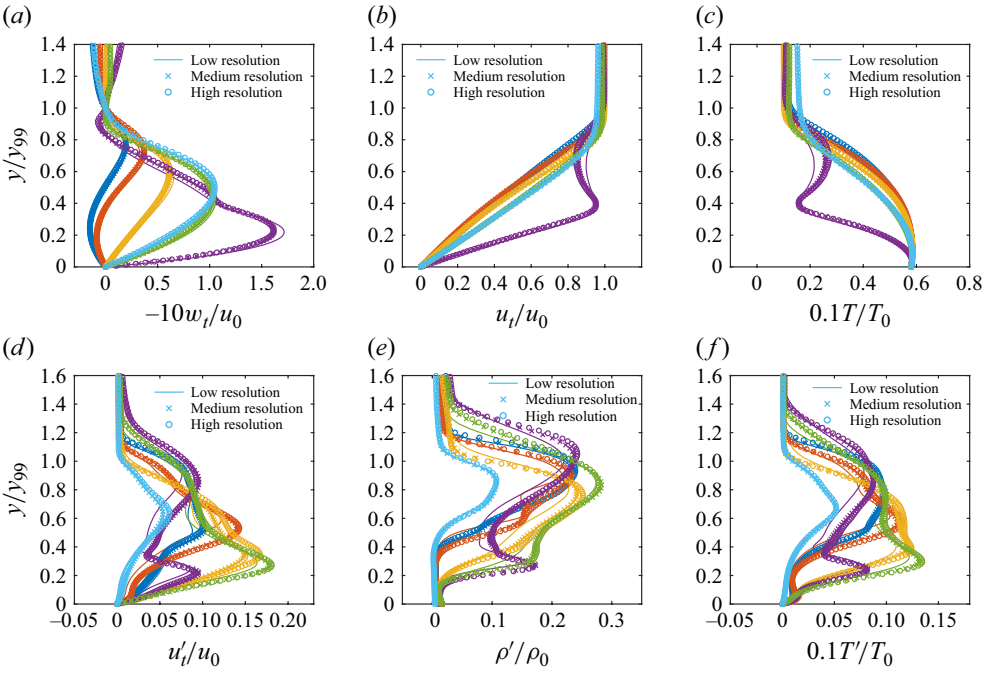


Figure 2. Mean-flow profiles of (*a*) cross-flow velocity, (*b*) streamwise velocity and (*c*) temperature profiles at different spanwise locations for $x = 200$ mm under three types of grids. Root-mean-square (RMS) profiles of (*d*) the streamwise velocity fluctuations, (*e*) density fluctuations and (*f*) temperature fluctuations at different spanwise locations for $x = 200$ mm under three types of grids. The six coloured curves correspond to spanwise locations $z = 15$, 25, 35, 45, 55 and 65 mm, shown in blue, orange, yellow, purple, green and light blue, respectively.

temperature. The tangential velocity and temperature profiles from the medium- and high-resolution grids are virtually indistinguishable across various spanwise locations (lines in different colours). However, noticeable deviations emerge in the low-resolution results, particularly at $z = 45$ mm (purple lines).

To assess the grid sensitivity of the disturbance field, figure 2(*d–f*) compares the wall-normal profiles of the RMS streamwise velocity, density and temperature fluctuations at $x = 200$ mm across the three grid resolutions. The profiles obtained from the medium- and high-resolution grids exhibit excellent agreement, whereas noticeable deviations emerge in the low-resolution results. Because the relative difference between the medium and high resolutions remains strictly bounded within 5 % across all considered variables, the medium-resolution grid is adopted to balance numerical accuracy with computational efficiency.

2.2. *Linear stability theory analysis*

The stability characteristics of the basic flow are then investigated using the linear stability theory (LST), in a manner similar to that in the study of Chen *et al.* (2017). The decomposition of the flow field is given by

$$q(x, y, z, t) = \bar{q}(y) + q'(y) = \bar{q}(y) + \hat{q}(y)\exp(i\alpha x + i\beta z - i\omega t) + \text{c.c.} \tag{2.1}$$

Here, $q = (u, v, w, T, p)$ and $\bar{q}$ denote the basic states, q' denotes the disturbance, $\hat{q}(y)$ is the shape function of the disturbance, α and β represent the streamwise wave numbers and

https://doi.org/10.1017/jfm.2026.11955 Published online by Cambridge University Press

the spanwise wave numbers, respectively, and ω is the angular frequency. In this study, the basic state is given by DNS and is partly presented in figure 2(*a–c*).

After substituting the decompositions given by (2.1) into the Navier–Stokes equations, subtracting the basic states, and neglecting the non-parallel and nonlinear terms, the following eigenvalue problem is obtained:

$$L_1(x, \alpha, \beta, \omega)\hat{q}(y) = 0 \tag{2.2}$$

where L_1 is a linear operator that has been described in previous literature (Chen *et al.* 2017) and the flow parameters are the same as in the experiment. When considering the temporal formula, we have

$$\omega = \omega(\alpha, \beta), \tag{2.3}$$

where ω is complex, and α and β are real. When considering the spatial formula, we have

$$\alpha = \alpha(\omega, \beta), \tag{2.4}$$

where α is complex, and ω and β are real. For the smooth-wall model, the boundary conditions are

$$\hat{u} = \hat{v} = \hat{w} = \hat{T} = 0 \quad \text{at} \quad y = 0 \quad \text{and} \quad \text{at} \quad y \to \infty. \tag{2.5}$$

The analysis in this study is carried out with the spatial formula using the in-house code in our laboratory; see the work of Chen *et al.* (2017) for the specific calculation method and code verification.

Figure 3(*a–c*) presents the spatial LST results at three discrete locations: L1 at $(x, z) = (150, 23)$ mm, L2 at $(x, z) = (180, 44)$ mm and L3 at $(x, z) = (200, 48)$ mm. The LST results at these locations exhibit qualitatively similar topologies, featuring distinct cross-flow (labelled C) and second modes (labelled S). At L1, the most unstable cross-flow mode occurs at approximately 50 kHz, whereas the second mode peaks near 135 kHz. At L2, the dominant frequencies shift to roughly 30 kHz for the cross-flow mode and 280 kHz for the second mode. Further downstream at L3, the cross-flow and second modes peak at approximately 35 and 230 kHz, respectively. Obviously, both the unstable frequency bandwidth and the maximum spatial growth rate of the second mode are significantly amplified at L2 compared with the other two locations, a consequence of local variations in the mean base flow. Figure 3(*d*) illustrates the streamwise evolution of the spatial growth rate for the two-dimensional second mode ($f = 230$ kHz, spanwise wavenumber $\beta = 0$) along the $z = 44$ mm plane. Upstream of $x = 150$ mm, the growth rate is negative, indicating that the mode is locally stable. Downstream of this position, the growth rate increases rapidly, attaining a maximum near $x = 180$ mm, before gradually declining while remaining strictly positive.

2.3. *Disturbance-injection strategy for DNS*

Guided by the LST results, a disturbance field comprising a spectrum of frequencies, spanwise wavenumbers and streamwise wavenumbers is introduced at the wall near the leading edge of the computational domain. Specifically, forcing frequencies of $\omega_1 = 2\pi \times 35$ kHz and $\omega_2 = 2\pi \times 50$ kHz are selected to excite travelling cross-flow waves, whereas $\omega_3 = 2\pi \times 140$ kHz and $\omega_4 = 2\pi \times 230$ kHz are chosen to trigger the second-mode instability. These perturbations are implemented via unsteady blowing and suction applied near the inflow boundary and along the leading edge of the compound delta wing (indicated by the blue regions D1 and D2 in figure 1*b*). The wall-normal disturbance velocity, v_n, is prescribed as

https://doi.org/10.1017/jfm.2026.11955 Published online by Cambridge University Press

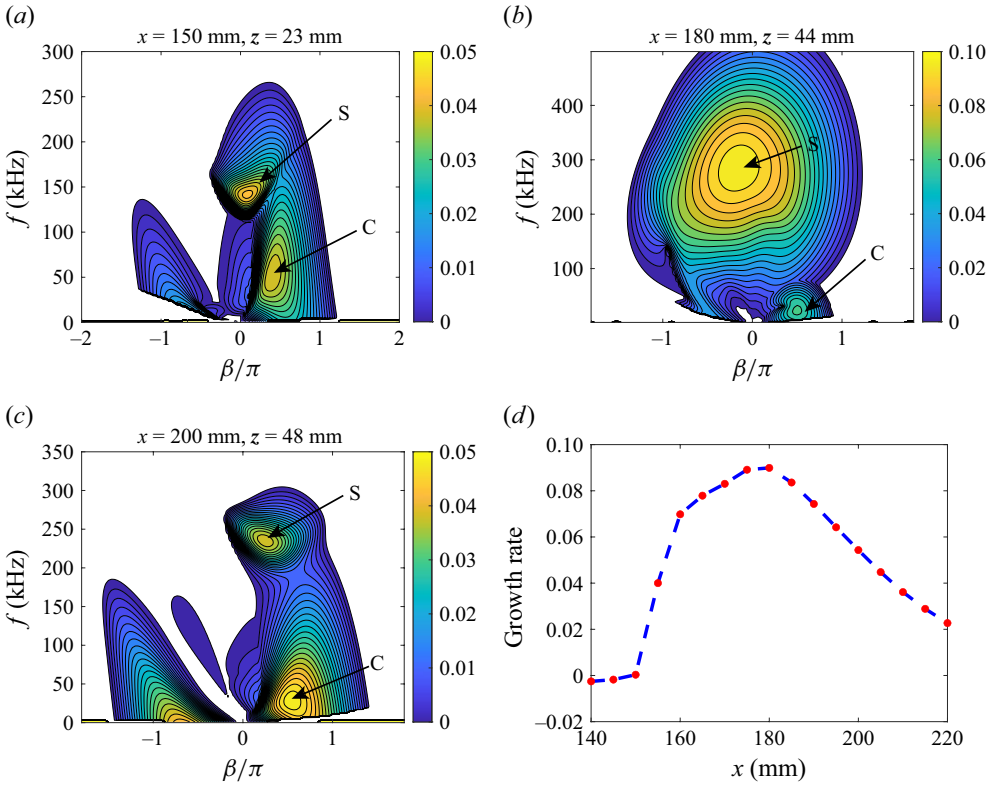


Figure 3. Variation of spatial growth rate $(-\alpha_i)$ with frequency and spanwise wave number at different positions: (*a*) $(x, z) = (150, 23)$ mm, (*b*) $(x, z) = (180, 44)$ mm, (*c*) $(x, z) = (200, 48)$ mm. (*d*) The evolution of the spatial growth rate $(-\alpha_i)$ of the second mode for $f = 230$ kHz and $\beta = 0$ by LST, along the streamwise plane $z = 44$ mm.

$$v_n = A v_{dis_x} v_{dis_z} v_{fre} v_{shape}, \tag{2.6}$$

$$v_{dis_x} = \frac{1}{50} \sum_{i=1}^{50} \sin\left(\frac{2\pi x}{L_i}\right), \tag{2.7}$$

$$v_{dis_z} = \frac{1}{30} \sum_{i=1}^{30} \sin\left(\frac{2\pi z}{L_i}\right), \tag{2.8}$$

$$v_{fre} = A_1 \sin(\omega_1 t) + A_2 \sin(\omega_2 t) + A_3 \sin(\omega_3 t) + A_4 \sin(\omega_4 t), \tag{2.9}$$

$$v_{shape1} = \sin^3\left(\frac{\pi(x - x_1)}{x_2 - x_1}\right), \tag{2.10}$$

$$v_{shape2} = \sin^3\left(\frac{\pi(k_z - k_{z1})}{k_{z2} - k_{z1}}\right) \sin\left(\frac{\pi(k_x - k_{x3})}{k_{x4} - k_{x3}} + \frac{\pi}{2}\right), \tag{2.11}$$

where x and z denote the streamwise and spanwise coordinates, respectively, t is time, and $L_i = i$ mm represents the wavelength in the streamwise or spanwise direction.

https://doi.org/10.1017/jfm.2026.11955 Published online by Cambridge University Press

The surface actuation is divided into two distinct spatial regions, modulated by the shape functions v_{shape1} and v_{shape2}. The first region aligns approximately with the intersection of the zone B inlet and the model surface, spanning the streamwise domain from $x_1 = 25$ mm to $x_2 = 45$ mm. The second region (shaded dark blue) runs parallel to the leading edge, covering the remaining streamwise extent and spanning the transverse grid indices from $k_{z1} = 270$ to $k_{z2} = 320$. The global actuation amplitude is set to $A = 1.0$, while the specific forcing amplitudes for the 35, 50, 140 and 230 kHz components are assigned as $A_1 = 1.2$, $A_2 = 1.0$, $A_3 = 0.5$ and $A_4 = 0.3$, respectively. The relative magnitudes of A1, A2, A3 and A4 are established based on the fact that higher-frequency disturbances tend to have relatively smaller initial amplitudes, similar to the disturbance introduction approach used in Guo *et al.* (2025).

For the subsequent analysis, based on our LST results and disturbance-injection strategy, the disturbance field is bandpass filtered to isolate the distinct instability mechanisms. Specifically, frequency bands of 220–240, 30–55 and 12–25 kHz are selected to extract disturbances that match the frequencies of the second mode, the cross-flow mode and the first mode in the boundary layer, respectively. Disturbances outside the boundary layer refer to those with the same frequencies as these modes. The 12–25 kHz bandwidth is specifically chosen to delineate the lower-frequency first mode from the cross-flow mode, consistent with the spectral characteristics detailed by Qiu *et al.* (2024).

3. Results

Based on previous observations of a prominent streak at $z = 44$ mm (Ullah *et al.* 2024), which is primarily composed of the second-mode instability (Huang *et al.* 2021; Feng *et al.* 2024), we analysed the compression–expansion effects in the shock-wave interaction region near the corner of the compound delta-wing to elucidate the mechanisms driving the growth of the instability. A defining characteristic of the second mode is its large velocity disturbance below the sonic line, induced by periodic compression–expansion motions (Zhu *et al.* 2016). Figure 4 presents the velocity divergence in the streak plane ($z = 44$ mm, see figure 1*a*) and an adjacent plane without a streak ($z = 50$ mm, see figure 1*b*). The compression–expansion disturbances associated with the second mode are observed to follow two distinct development paths (indicated by arrows of different colours): (i) disturbances that propagate downstream within the boundary layer, and (ii) disturbances that originate near the leading edge, propagate toward the bow shock and are subsequently reflected back into the boundary layer. These two paths corporately excite the internal boundary-layer second mode. At $z = 44$ mm, the second mode exhibits earlier growth and larger amplitudes (compared to other streamwise planes, see Ullah *et al.* 2024 and figure 5*b*), attributable to the locally thicker boundary layer and the additional energy injection from this newly identified reflection path. A similar but weaker phenomenon exists at $z = 50$ mm, indicating this mechanism is widespread. In the subsequent discussion, we will focus on the plane at $z = 44$ mm.

The reflection-induced excitation path represents a previously unreported receptivity mechanism in hypersonic boundary layers. To isolate its contribution, the density field at $z = 44$ mm is bandpass filtered in the range of $220 - 240$ kHz to extract disturbance at the second-mode frequency (figure 5*a*). In practice, we used the Filtfilt filtering function in MATLAB to obtain a filtered time series without phase shift with a Butterworth filter to generate the filter coefficients. Within the highlighted region (indicated by the cyan square), the filtered density perturbations exhibit a highly regular spatial structure, clearly tracing the shock-reflection propagation path. Downstream of this region, the spatial extent of the disturbance expands rapidly. Figure 5(*b*) shows the streamwise long-term amplitude

https://doi.org/10.1017/jfm.2026.11955 Published online by Cambridge University Press

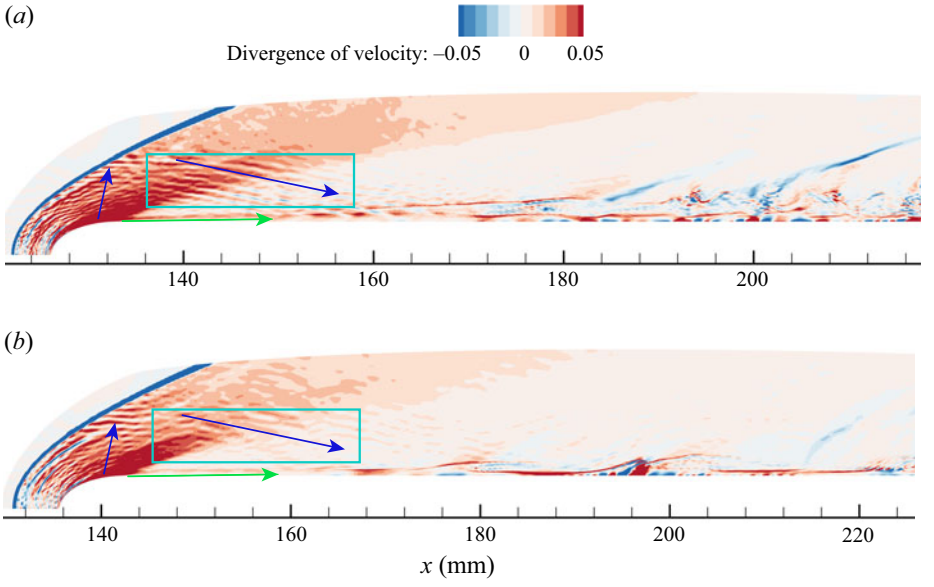


Figure 4. The distribution of divergence of velocity $\theta = \nabla \cdot \boldsymbol{u}$ at two spanwise planes. (*a*) $z = 44$ mm. (*b*) $z = 50$ mm. Arrows in different colours represent different disturbance propagation paths.

variation of the internal second-mode disturbance (the maximum value in boundary layer), revealing a localised amplification near $x = 150$ mm, which precisely coincides with the location where the reflected disturbances re-enter the boundary layer (see the arroe labelled as critical point). Compared to the amplitude evolution predicted by LST, the amplitude of the second mode obtained by DNS shows a significant increase after $x = 150$ mm, indicating the presence of a new disturbance excitation mechanism. In contrast, the growth of the second-mode disturbance at $z = 50$ mm, where the reflection–penetration event is weaker, is relatively slow. Figure 5(*c*) presents a comparison between the short-term (denoted ST-RMS1 and ST-RMS2) and long-term (denoted LT-RMS) statistically averaged amplitudes near $x = 150$ mm (the green square in figure 5*b*). The amplitude is obtained by calculating the RMS of the variable, i.e.

$$|A| = \sqrt{\frac{1}{N}\sum_{i=t_1}^{t_N} \hat{q}_i^2}, \tag{3.1}$$

where $N = 800$ and $N = 60$ (covering more than 10 periods of the second mode) for long- and short-term statistics, respectively. It can be observed that within the region affected by this receptivity mechanism, the short-term averaged amplitude exhibits a stepwise (rather than monotonic) rise, indicating strong discrete modulation by the reflected path.

To quantify how the reflected disturbances modulate the internal boundary-layer waves, local phase and amplitude analyses are performed at three discrete points in figure 5(*a*) (see the insert). Points 1 and 3 are located on the primary internal propagation path, while point 2 lies on the reflection path immediately prior to its re-entry. Disturbances from point 1 and point 2 eventually converge at point 3 for each location. A correlation parameter K is introduced to characterise the phase difference between the two interacting disturbances:

https://doi.org/10.1017/jfm.2026.11955 Published online by Cambridge University Press

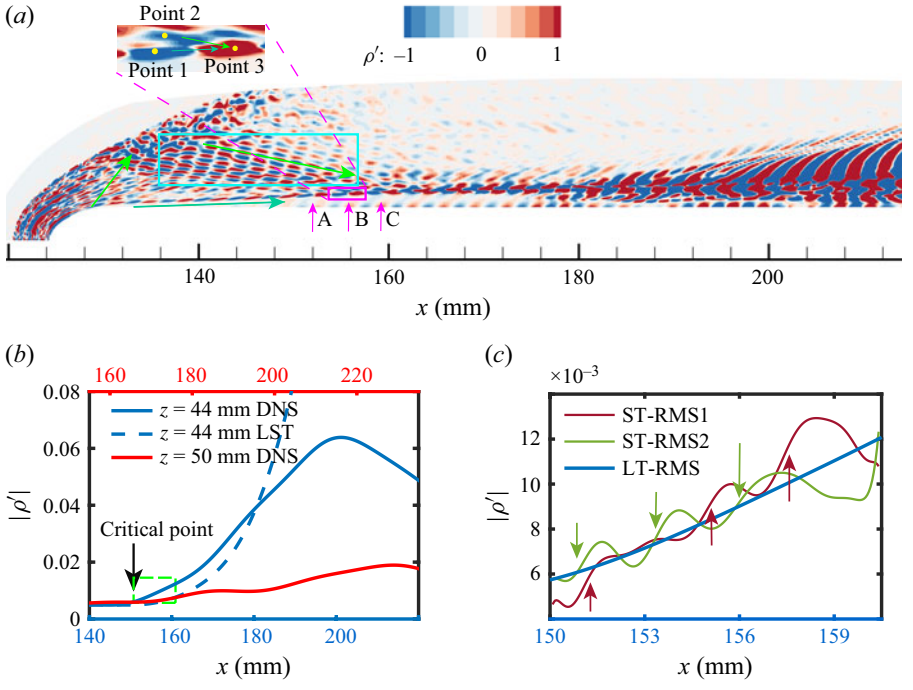


Figure 5. (*a*) Distribution of the second-mode frequency disturbance represented by ρ' at plane $z = 44$ mm, obtained by bandpass filtering and normalised by a specific value. (*b*) Evolution of the long-term statistical amplitude of the second-mode frequency disturbance within the boundary layer at plane $z = 44$ mm and $z = 50$ mm, denoted by the maximum value in boundary layer and normalised by free stream density. The blue dashed line represents the amplitude evolution of the second mode predicted by LST (figure 3*d*) at plane $z = 44$ mm. (*c*) Comparison of the long-term statistical amplitude (denoted as LT-RMS) and the short-term statistical amplitudes for disturbance starting from two different time instants (denoted ST-RMS1 and ST-RMS2), showing the green dashed box region in *b*.

$$K = \frac{\sum_{i=t_1}^{t_N} \hat{p}_i \hat{q}_i}{|\hat{p}||\hat{q}|}, \tag{3.2}$$

where $\hat{p}_i$ and $\hat{q}_i$ represent the time-series values of the two variables (here for point 1 and point 2), and $|\cdot|$ denotes the short-term statistical amplitude (given in (3.1)). It can be shown that $K = 1$ denotes exactly in-phase and $K = -1$ denotes totally antiphase. Figure 6(*a*) presents the instantaneous growth rate (the short-term amplitude ratio between point 3 and point 1) of the second mode against K at the three locations within the reflection–penetration region (A, B and C in figure 5*a*). Each location has data from three points, resulting in a total of nine data points. Different scatter points are obtained by varying the initial time (t_1 in (3.2)) while keeping the statistical time (N in (3.2)) constant. The data demonstrate a clear positive correlation: higher phase alignment (larger K) between the reflected and internal paths yields a larger instantaneous growth rate of the internal disturbance. Figures 6(*b*) to 6(*d*) illustrate the temporal evolution for three representative cases – antiphase ($K = -0.98$), alternating phase ($K = 0.07$) and in-phase ($K = 0.90$) – corresponding to instantaneous growth rates of 1.03, 1.18 and 1.42, respectively. These findings confirm that the reflected disturbances strongly modulate and amplify the internal boundary-layer waves based on their relative phase alignment. And they share similarities with the phase-locked mechanism proposed by Li *et al.* (2020) and

https://doi.org/10.1017/jfm.2026.11955 Published online by Cambridge University Press

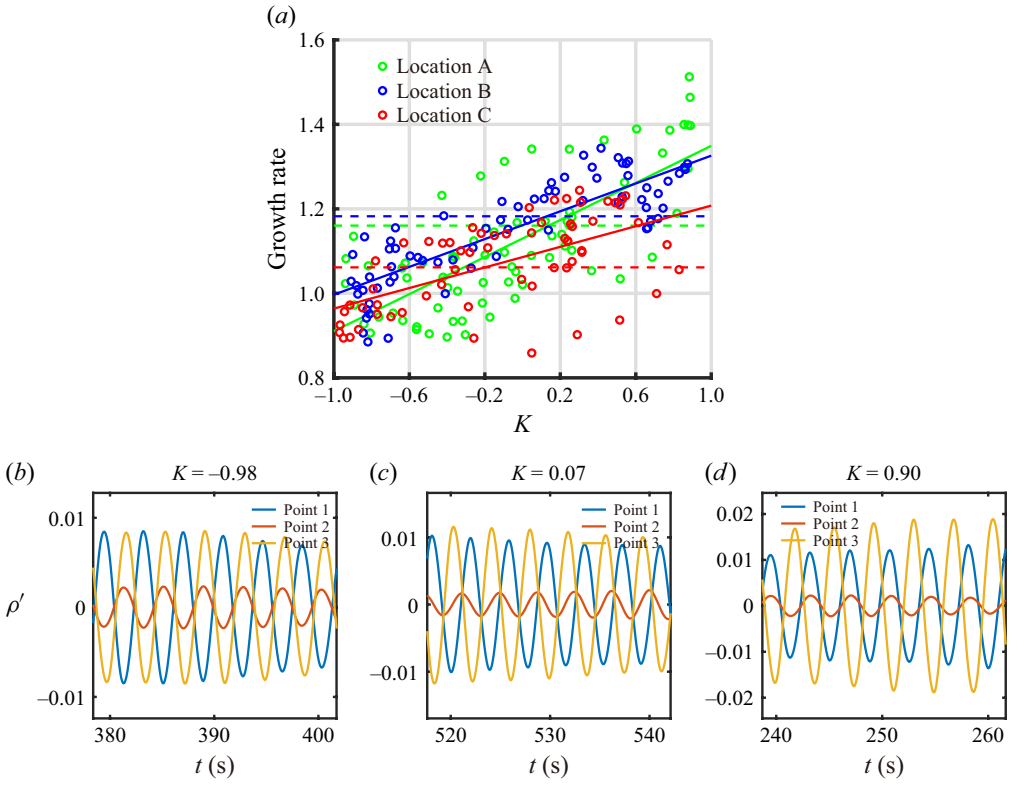


Figure 6. (*a*) Scatter plot and trend of the K value versus the instantaneous growth rate of the second mode within the boundary layer at three locations (i.e. A, B, C) in figure 5(*a*). The dashed line represents the long-term statistical average growth rate for each location. (*b–d*) Time series of disturbances at the three points corresponding to different typical K values, normalised by free stream density. The three points are adjacent points on the two paths in figure 5(*a*). The instantaneous growth rate is obtained from the ratio of disturbance amplitudes at point 3 and point 1.

Zhang *et al.* (2020). The reason for the stepwise growth observed in figure 5(*c*) is that different streamwise positions exhibit varying phase relationships. When disturbances on the two paths meet and are in phase, the growth rate of disturbance amplitude within the boundary layer increases more strongly (see the arrow in figure 5*c*). Note that the phase relationship varies over time under long-term observation but can maintain a phase-locked state over short periods at a given location. Ultimately, under long-term statistical averaging, the amplitude growth curve becomes smooth, as shown in figure 5(*c*).

The spatial topology of this mechanism is further investigated in figure 7, providing a three-dimensional perspective of the reflection path. To better demonstrate the three-dimensional characteristics of the path, two viewing perspectives are provided, as shown in figures 7(*a*) and 7(*b*). The presented location is in the cyan box region in figure 1(*a*). The three streamwise planes ($z = 44$, 57 and 67 mm) indicate the approximate planes along which the disturbance paths lie following their reflection by the shock wave. The colour mapping along these paths (red tubular structures) denotes the wall-normal coordinate (y), with redder hues corresponding to greater wall-normal heights. Across multiple spanwise locations, the paths share identical characteristics: originating from the wall, radiating obliquely forward, interacting with the bow shock and reflecting back towards the wall (see the red arrows). In particular, the forward-propagating path is curved prior to the shock

https://doi.org/10.1017/jfm.2026.11955 Published online by Cambridge University Press

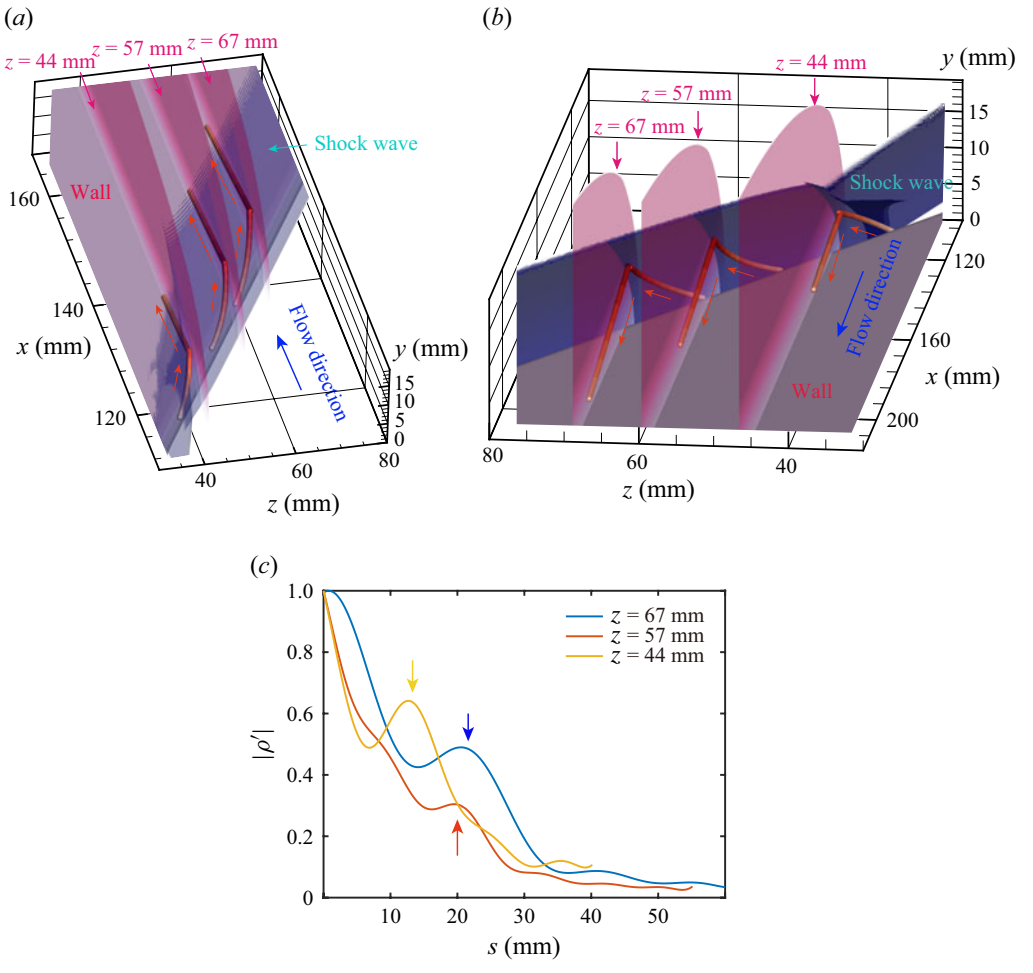


Figure 7. Propagation path of the second-mode frequency disturbance from two viewing perspectives: (*a*) front view, (*b*) end view. The views correspond to the blue box region in figure 1(*a*). (*c*) Evolution of the disturbance amplitude along the propagation path, quantified by the density perturbation and normalised by its maximum value. The relative locations of $z = 44$, 57 and 67 are shown in figure 1(*a*) for reference.

interaction, likely due to the intense mean-flow gradients near the leading edge, whereas the reflected path is nearly straight. The amplitude evolution of the density disturbances along these paths (figure 7*c*, starting from the corresponding leading edge with $s = 0$) is also consistent: an initial rapid decay as the newly generated disturbance adjusts to the spatial propagation characteristics, followed by a slight amplification upon reaching the shock wave (see arrows in figure 7*c*) and a gradual decay along the reflected path. Crucially, the disturbance retains sufficient amplitude upon re-entering the boundary layer to effectively modulate the internal flow, which can also be observed in figure 5(*a*).

Finally, we evaluate the mechanism's influence on low-frequency instabilities, specifically the first mode ($12 - 25$ kHz) and cross-flow mode ($30 - 55$ kHz), by bandpass filtering the density field, as shown in figure 8. Although the geometric reflection paths exist, the low-frequency disturbances do not actively propagate along them. Instead, after generation near the leading edge, they propagate almost directly downstream (not strictly along the streamwise plane), conforming to the shock curvature

https://doi.org/10.1017/jfm.2026.11955 Published online by Cambridge University Press

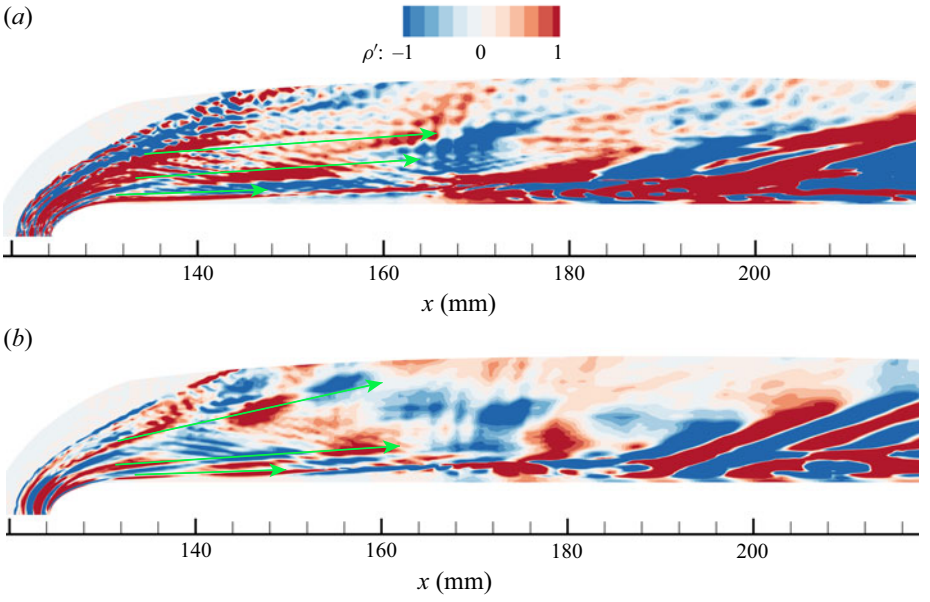


Figure 8. Distribution of density fluctuations at $z = 44$ mm for (*a*) first-mode (12–25 kHz) and (*b*) cross-flow-mode (30–55 kHz) disturbances, normalised by a specific value.

and remaining entirely unaffected even when traversing the reflection paths. This indicates that the shock-reflection receptivity mechanism is highly selective, exerting minimal influence on low-frequency modes, likely due to poor coupling between their longer wavelengths and the spatial scales of the reflection path. A comprehensive physical explanation for the diminished sensitivity of this mechanism to longer-wavelength disturbances needs further investigation.

4. Discussion

This receptivity mechanism reveals a distinct physical path for the evolution of high-frequency disturbances in hypersonic boundary layers. Contrary to the traditional paradigm where disturbances propagate downstream from the leading edge, this mechanism exhibits a more complex spatial interaction. Specifically, disturbances originating near the wall radiate obliquely forward into the upstream and outer boundary-layer regions. Upon penetrating the boundary layer and entering the postshock flow, these forward-propagating disturbances interact strongly with the bow shock. The shock wave effectively acts as a reflecting spectral mirror for high-frequency waves, altering their propagation direction and reflecting them back into the boundary layer. The influence of the identified reflection mechanism on transition onset manifests as an enhanced initial amplification of second-mode instabilities. Furthermore, this mechanism seems to be sensitive to the shock-layer topology, suggesting that it may play a more decisive role in complex three-dimensional geometries, where geometric curvatures and shock-wave orientations may favour stronger acoustic-instability coupling.

Historically, this mechanism has likely been overlooked for two primary reasons. First, the disturbance propagation path closely coincides with the spatial location of the Mach waves. These Mach waves, generated by the leading-edge curvature, propagate toward the shock wave, providing a conduit for disturbances to evolve and subsequently reflect

https://doi.org/10.1017/jfm.2026.11955 Published online by Cambridge University Press

back into the boundary layer. For the present compound delta-wing model, the reflection phenomenon becomes highly prominent downstream of the conner of the compound delta-wing. This spatial dependence indicates that the effective range and intensity of the mechanism are highly sensitive to the free stream Mach number and leading-edge geometric parameters, such as the bluntness radius and sweep angle. Consequently, under typical flow conditions, the spatial footprint of this mechanism remains relatively localised, rendering it easily unnoticeable – although subtle traces of similar wave reflections appear to exist, yet unaddressed, in recent numerical results (e.g. figure 6*d* by Guo *et al.* 2025).

Second, the mechanism's highly selective nature inherently obscures its observation. It exerts a significant modulatory effect exclusively on high-frequency instabilities (e.g. the second mode), while its influence on low-frequency modes (e.g. cross-flow and first modes) is relatively minor. In typical hypersonic flow fields, low-frequency disturbances naturally possess larger initial amplitudes in the free stream and thus are more readily observed. In contrast, high-frequency disturbances exhibit almost negligible amplitudes near the leading edge, making their subsequent propagation and reflection far more difficult to detect.

Furthermore, it is important to distinguish this shock-reflection path from the receptivity mechanism reported by Wan *et al.* (2020), where the second-mode frequency disturbance enters the boundary layer by propagating along the entropy layer. In contrast, the current mechanism dictates that disturbances generated near the leading edge propagate downstream in a multichannel mode, characterised by radiation angles that are significantly steeper than the shallow immersion angle associated with the entropy layer. It should be noted that the acoustic wave propagation reported by Chuvakhov *et al.* (2021) exhibits phenomenological similarities to the mechanism described herein, particularly regarding the role of shock-wave reflections. However, the physical drivers and spectral focus of the two studies are distinct. While Chuvakhov *et al.* (2021) investigated the receptivity of the boundary layer to external particulates – resulting in multiple reflections and the excitation of the first mode – the present study identifies a discrete, single-reflection pathway for disturbances originating at the wall. Crucially, we demonstrate that this mechanism exerts a potent modulatory effect on high-frequency instabilities, specifically the second mode, representing a transition pathway that has not been previously characterised in this configuration.

5. Conclusions

In this work, a new receptivity mechanism for the second mode in hypersonic flow was identified. The results reveal a distinct physical path in which disturbances originating at the wall radiate obliquely forward, interact with the bow shock and are subsequently reflected back into the boundary layer. Upon re-entry, these reflected waves significantly modulate and amplify the internal boundary-layer disturbances within the interaction region, triggering a localised surge in amplitude followed by enhanced modal growth of the second mode. A phase-locked mechanism between the reflection and internal modes is involved in these interactions.

Furthermore, this shock-reflection mechanism exhibits strong frequency selectivity; it profoundly influences high-frequency instabilities, such as the second mode, while exerting a negligible effect on low-frequency modes, including cross-flow and first-mode disturbances. This selectivity is probably attributed to the longer wavelengths of low-frequency modes, which couple poorly with the spatial scales of the reflection path.

https://doi.org/10.1017/jfm.2026.11955 Published online by Cambridge University Press

Ultimately, the discovery of this receptivity mechanism occurring downstream of a leading edge provides new insight into the role of shock waves in hypersonic boundary-layer transition. Although this mechanism may be relatively weak in most practical environments, the underlying physical principles it reveals and its potential engineering applications – particularly in active flow control – are of considerable significance. It further highlights how leading-edge disturbances drive instability development during near-wall transition.

Supplementary movies. Supplementary movies are available at https://doi.org/10.1017/jfm.2026.11955.

Funding. This work was supported by the National Natural Science Foundation of China (grant nos 12072002, 109103010062, 10921202) and National Key Project (GJXM92579).

Declaration of interests. The authors report no conflict of interest.

References

CHEN, S., DENG, X. & LEE, C. 2026 Soliton-like coherent structures: a key to opening the door to turbulence. *Natl Sci. Rev.* **13** (2), nwaf535.

CHEN, X., ZHU, Y. & LEE, C. 2017 Interactions between second mode and low-frequency waves in a hypersonic boundary layer. *J. Fluid Mech.* **820**, 693–735.

CHUVAKHOV, P.V., FEDOROV, A.V. & POGORELOV, I.O. 2021 Numerical simulation of boundary layer receptivity to solid particulates near a blunt leading edge. *AIP Conf. Proc.* **2351** (1), 030026.

FEDOROV, A.V. 2011 Transition and stability of high-speed boundary layers. *Annu. Rev. Fluid Mech.* **43**, 79–95.

FEDOROV, A.V. & KHOKHLOV, A.P. 1991 Excitation of unstable modes in a supersonic boundary layer by acoustic waves. *Fluid Dyn.* **26**, 531–537.

FENG, Z., CAI, C., LEE, C. & YANG, D. 2024 Investigation of an overlap of heating peaks in the hypersonic boundary layer over a blunt cone. *Phys. Rev. Fluids* **9**, L071901.

GOLDSTEIN, M.E. 1985 Scattering of acoustic waves into Tollmien–Schlichting waves by small streamwise variations in surface geometry. *J. Fluid Mech.* **154**, 509–529.

GUO, P. 2025 Transition reversal over a blunt plate at Mach 5. Part 2. The role of free-stream-disturbance form. *J. Fluid Mech.* **1025**, A54.

GUO, P., HAO, J. & WEN, C. 2025 Transition reversal over a blunt plate at Mach 5. *J. Fluid Mech.* **1005**, A5.

HUANG, G., SI, W. & LEE, C. 2021 Inner structures of Görtler streaks. *Phys. Fluids* **33** (3), 034116.

LEE, C. & CHEN, S. 2019 Recent progress in the study of transition in the hypersonic boundary layer. *Natl Sci. Rev.* **6** (1), 155–170.

LEE, C. & JIANG, X. 2019 Flow structures in transitional and turbulent boundary layers. *Phys. Fluids* **31** (11), 111301.

LI, C., ZHANG, Y. & LEE, C. 2020 Influence of glow discharge on evolution of disturbance in a hypersonic boundary layer: the effect of first mode. *Phys. Fluids* **32** (5), 051701.

MASLOV, A.A., SHIPLYUK, A.N., SIDORENKO, A.A. & ARNAL, D. 2001 Leading-edge receptivity of a hypersonic boundary layer on a flat plate. *J. Fluid Mech.* **426**, 73–94.

MCKENZIE, J.F. & WESTPHAL, K.O. 1968 Interaction of linear waves with oblique shock waves. *Phys. Fluids* **11** (11), 2350–2362.

MORKOVIN, M.V. 1969 On the many faces of transition. In *Viscous Drag Reduction* (ed. C.S. Wells), pp. 1–31. Springer US.

QIU, H., SHI, M., ZHU, Y. & LEE, C. 2024 Boundary layer transition of hypersonic flow over a delta wing. *J. Fluid Mech.* **980**, A57.

SARIC, W.S., REED, H.L. & KERSCHEN, E.J. 2002 Boundary-layer receptivity to freestream disturbances. *Annu. Rev. Fluid Mech.* **34**, 291–319.

ULLAH, H., QIU, H., YU, G., KHAN, M. & LEE, C. 2024 Exploring the boundary layer transition of hypersonic flow over a compound delta wing. *Phys. Fluids* **36** (3), 035174.

WAN, B., SU, C. & CHEN, J. 2020 Receptivity of a hypersonic blunt cone: role of disturbances in entropy layer. *AIAA J.* **58**, 1–8.

YANG, C., FENG, Z. & LEE, C. 2025 Self-organized oblique waves upstream of the leading edge of a flat plate. *Phys. Fluids* **37** (2), 021714.

ZHANG, Y., LI, C. & LEE, C. 2020 Influence of glow discharge on evolution of disturbance in a hypersonic boundary layer: the effect of second mode. *Phys. Fluids* **32** (7), 071702.

https://doi.org/10.1017/jfm.2026.11955 Published online by Cambridge University Press

ZHONG, X. & WANG, X. 2012 Direct numerical simulation on the receptivity, instability, and transition of hypersonic boundary layers. *Annu. Rev. Fluid Mech.* **44**, 527–561.

ZHU, Y., ZHANG, C., CHEN, X., YUAN, H., WU, J., CHEN, S., LEE, C. & GAD-EL HAK, M. 2016 Transition in hypersonic boundary layers: role of dilatational waves. *AIAA J.* **54** (10), 3039–3049.

https://doi.org/10.1017/jfm.2026.11955 Published online by Cambridge University Press